$Fe_xBi_2Se_3$ superconductivity, dimensional transport, and high electron mobility are associated with the natural nanostructure of Bi_2Se_3 single crystals

Jan Zich,[1] Martin Míšek,[2] Václav Holý,[3,4] Karel Carva,[3] Jakub Čížek,[3] Jiří Navrátil,[1,2] Patrik Čermák,[1] Petr Knotek,[1] Kateřina Čermák Šraitrová,[1] Stanislav Cichoň,[2] Jiří Hejtmánek,[5] Zdeněk Jirák,[5] and Čestmír Drašar[1,*]

[1]*University of Pardubice, Faculty of Chemical Technology, Studentska 573, 53210 Pardubice, Czech Republic*
[2]*Institute of Physics, Czech Academy of Sciences, Na Slovance 2, 182 21 Prague 8, Czech Republic*
[3]*Department of Condensed Matter Physics, Faculty of Mathematics and Physics, Charles University, Ke Karlovu 3, 121 16 Praha 2, Czech Republic*
[4]*Masaryk University, Department of Condensed Matter Physics, Kotlarska 2, 61137 Brno, Czech Republic*
[5]*FZU–Institute of Physics of the Czech Academy of Sciences, Cukrovarnická 10/112, 162 00 Prague 6, Czech Republic*

(Received 9 March 2023; revised 2 August 2023; accepted 11 September 2023; published 28 September 2023)

In this paper, we report the physical properties of $Fe_xBi_2Se_3$ single crystals. Fe-intercalated Bi_2Se_3 exhibits superconductivity, pronounced Shubnikov–de Haas oscillations, high carrier mobility, and features of two-dimensional (2D) transport in the sample volume for x as low as 0.02. The superconductivity of the samples is limited to the range $x = 0.02$–0.04. We correlate all the transport properties with structural properties, namely, with mosaic structure of single crystals and point defects. This correlation in the context of the rich literature data allows us to build an intricate physical picture addressing the unique properties of the material under study within the framework of the Bi_2Se_3 quasi-2D defect structure model. The ultimate aim of this paper is to show that many interesting properties of Bi_2Se_3 may be associated with inhomogeneous distribution of defects in the volume of the sample, which largely replicates the mosaicity of single crystals.

DOI: 10.1103/PhysRevB.108.125308

I. INTRODUCTION

Bi_2Se_3 is a narrow gap semiconductor that has been studied comprehensively over a long period. Its thorough exploration as one of the best thermoelectric (TE) materials started in the 1950s [1]. Later, at the turn of the millennium, magnetic order induced by transition metals attracted much attention in the search for diluted magnetic semiconductors [2]. Its further rediscovery was related to nontrivial topology in electronic states at interfaces. The fact that it belongs to three-dimensional (3D) topological insulators with one distinctive Dirac cone within the surface states triggered an enormous research effort [3,4]. This was accompanied by a wide variety of doping studies aimed at revealing the interference of magnetic/nonmagnetic impurities with topological surface states (TSS) in general. Within these studies, a couple of dopants proved to induce an unconventional (nematic) superconductivity (SC) [5–7]. Recently, the dimensionality of charge transport has been widely discussed; 2D electronic transport is documented by the presence of quantum Hall plateaus in doped and undoped Bi_2Se_3 [8–11]. The abundance of intriguing properties of Bi_2Se_3 seems to be inexhaustible. Hence, the fine mechanisms underlying this richness call for further experimental endeavor. In this paper, we introduce another member of the family exhibiting features of superconductivity and 2D transport involving TSS ("bulk quantum Hall effect"), which could exhibit the SC state due to pairing of Dirac electrons [12]. Two-dimensional transport [8] and a weak hint of SC behavior [13] for heavily doped samples were reported recently, though not within the same sample or batch. Two-dimensional transport has been discussed in Bi_2Se_3 in general for undoped Bi_2Se_3, eventually concluding with 3D transport [10,11].

The prepared $Fe_xBi_2Se_3$ single crystals show a rather high concentration of free electrons up to $\approx 10^{20}\,\mathrm{cm}^{-3}$ (similar to Cu- and Nb-doped samples [14,15]). However, unlike other SC Bi_2Se_3 systems, Fe-intercalated samples retain unexpectedly high mobilities, especially in the low-temperature region. This indicates either healing of the structure or an antilocalization effect in general. SC evidenced by a drop of longitudinal resistivity to zero appears even at a dopant concentration as low as $x = 0.02$, which contrasts with other SC family members. The lowest content of dopant is reported for Sr with $x \approx 0.06$ while it is $x \approx 0.15$–0.25 for Cu and Nb. Another difference between Fe doping and Cu/Nb/Sr doping is that no Meissner effect is evident in Fe-doped samples (Fig. S8 in the Supplemental Material [16]), although resistive transitions are observed; in Cu/Nb/Sr-doped samples, the Meissner effect may not be complete but it is measurable [17–19]. The shielding fraction could thus be very low. The corresponding jump in heat capacity associated with the transition to the SC phase can be very small, as shown for the $Sr_xBi_2Se_3$ system [20]. Although measurable in our case, the jump in heat capacity is not associable with the SC state (see Secs. F and G of the Supplemental Material (SM) [16]). The simultaneous absence of the Meissner effect and the heat capacity jump may be related to the specific defect structure of $Fe_xBi_2Se_3$,

*cestmir.drasar@upce.cz

as discussed below. Regarding SC, the position of doping atoms in the structure is a subject of debate, with the van der Waals (vdW) interstitial position mostly reported [5,18]. The scanning tunneling microsope (STM) topography even suggests the formation of Sr clusters in [12]; a recent paper on Sr-doped Bi_2Se_3 strongly suggests substitution of Sr for Se1 in the bulk [21]. The unforeseen location Sr_{Se1} of the doping species completely changes the viewpoint on doping in this class of materials. We therefore also assume substitution of Fe for Se, i.e., formation of Fe_{Se} next to Fe interstitials Fe_i, which preserves the mutual agreement of all experimental findings. In the prepared $Fe_xBi_2Se_3$ single crystals we also observe features of 2D transport. To our knowledge, 2D transport and its topological nature in Bi_2Se_3 was first discussed in [22]. In contrast to this source, we argue that in properly doped $Fe_xBi_2Se_3$ the 3D charge transport is mixed with the 2D one and most likely involves TSS.

In the present paper, we attempt to shed more light on the interplay of the SC state, 2D transport, and high mobility with (native) defect structure that is modified by Fe doping. The Fe-induced defects cannot explain some experimental findings in undoped samples, e.g., 2D electronic transport documented by the presence of quantum Hall plateaus [8–11]. Therefore, we propose the involvement of native defects (e.g., antisites). All our findings and relevant published experimental and theoretical data clearly show that, in some cases, defects preferentially concentrate in a certain way along the vdW gap of the Bi_2Se_3 structure forming a topologically trivial (TT) layer within a topologically nontrivial (TnT) matrix, which results in alternating stacking of TnT and TT layers. Our data suggest that the stacking largely replicates the domain structure of single crystals, which has so far been overlooked when correlating physical properties with structure. Logically, the alternation of TnT and TT layers due to doping increases the participation of TSS in charge transport, thereby creating topologically based states in the bulk of the crystal. Moreover, such a "mosaiclike" structure naturally induces the features of 2D transport that are also present in some undoped but defect-rich Bi_2Se_3 samples [9,10]. The 2D character is also manifested in the lattice properties by a reduction in heat capacity due to Fe doping. Importantly, such a defect structure allows high carrier mobility. We document the physical picture on the $Fe_{0.02}Bi_2Se_3$ sample with the most prominent features (another sample in Sec. D of the SM [16]). Although each piece of evidence may seem to be incomplete, taken together they form a solid basis for our model: a two-phase layered "nanocomposite" model from an electronic point of view. The ultimate aim of this paper is to show that, for example, high mobility (SdH effect), 2D transport features, differences in carrier concentration obtained from SdH and Hall measurements, or superconductivity of Bi_2Se_3 may be associated with inhomogeneous distribution of defects in the volume of the sample.

II. EXPERIMENT

A. Crystal growth

Fe-doped single crystals of nominal composition $Fe_xBi_2Se_3$ ($x = 0$, 0.005, 0.01, 0.02, 0.04, 0.1) and $Bi_{2-x}Fe_xSe_3$ ($x = 0.005$ and 0.01) were grown using the free melt crystallization (FMC) method. Quartz ampoules containing elemental Bi and Se (of 5N purity, Merck) and compound $FeSe_{1.04}$ (presynthesized, Fe of 4N, Merck) at the desired stoichiometry were evacuated ($p < 10^{-3}$ Pa) and sealed. The crystal growth was performed by cooling in a horizontal furnace from 1073 to 823 K at a rate of 6 K/h. The crystals were then annealed at 823 K for 350 h and quenched in air. Undoped single crystals were grown using the same procedure. This FMC procedure produces single crystals 10–40 mm in length, 3–6 mm wide, and up to 3 mm thick. The samples are stable in air and do not change their parameters upon cycling within the measured temperature range. For the physical property measurements, FMC specimens with dimensions of (6–15) × 3 × (0.1–0.5) mm^3 were cut from the single crystals (Sec. D of the SM [16]).

Note: It can be assumed that the doping results may depend mainly on the dopant concentration and the overall stoichiometry of the host structure. However, we note that the method of preparation and the temperature at which equilibrium was reached (823 K) are at least as important as stoichiometry and dopant concentration. Thus the crystals investigated in this article are not comparable to other crystals prepared by the Bridgman method or epitaxially grown samples [23,24].

B. Transport and magnetotransport measurements

All transport properties were measured using the PPMS 14T apparatus (Quantum Design, Ltd.), temperature range 2–300 K, magnetic field up to 14 T. A ^{3}He insert was used to reach temperatures down to 0.5 K, where needed. Two separate pieces of the same material were used in a single run (i.e., identical B, T conditions) with 4 W resistivity and Hall bar geometry, respectively. The majority of measurements were done with the orientation of the magnetic field along the crystallographic c axis, i.e., perpendicular to the "easy-cleaving" planes of the vdW structure. In some specific cases, the horizontal rotator was used, allowing the rotation in the a-c plane. In this case, samples were placed on the measurement platform so that the current direction would lie in the plane of rotation. The ac magnetic susceptibility between 0.4 and 5 K was measured using PPMS with a ^{3}He option [25]. The Hall carrier concentration was obtained by symmetrizing Hall voltages for opposite B-field orientations. Heat capacity was measured using the same PPMS apparatus.

C. XRD—structural analysis

The goal of the high-resolution x-ray diffraction (HRXRD) experiments was to confirm the overall crystallographic quality of the samples and to determine the distances Se1-Se1, Se1-Bi, and Bi-Se2 of the basal planes and reveal the domain structure of single crystals. The measurements were carried out on a Rigaku SmartLab x-ray diffractometer equipped with a 9 kW Cu $K\alpha$ rotating anode (45 kV/200 mA). The HRXRD setup with a parabolic multilayer mirror and a 2 × 220 Ge channel-cut monochromator on the primary side and a one-dimensional detector was used for the measurement of long symmetric $2\Theta/\omega$ scans and reciprocal-space maps. The reciprocal-space maps were measured around the 000 15 and

000 27 reciprocal-lattice points. Additionally, we employed a low-resolution XRD setup (LRXRD) without a monochromator on the primary side and with a large two-dimensional detector; in this arrangement we measured large reciprocal-space maps comprising several dozens of reciprocal-lattice points. The goal of this measurement was to exclude the presence of other possible superconducting phases Fe_xSe_y (SM [16]).

D. DFT

Density functional theory (DFT) calculations were based on the full-potential linear augmented plane wave (FPLAPW) method, as implemented in the band structure program ELK [26]. The generalized gradient approximation (GGA) parametrized by Perdew-Burke-Ernzerhof [27] was used to determine the exchange-correlation potential. Spin-orbit coupling (SOC) provides a significant contribution in Bi-based compounds and was included in the calculation.

Fe_i was studied by embedding Fe at the interstitial site in the center of the vdW gap within a $2 \times 2 \times 1$ supercell (SCL) composed from standard hexagonal cells [28]. For Fe_{Bi} and Fe_{Se1} we used a modified supercell spanning within each layer 4×4 repetitions of each atom and in the perpendicular direction, one quintuple (QL).

The standard hexagonal cell has a very high c/a ratio of 6.9, and for the $2 \times 2 \times 1$ SC atoms in each plane form an artificial period of 2, while vertically there is an unnecessarily large period of three whole quintuples separated by weak interaction via the vdW gap. Such a choice appears to be appropriate for Fe_i where it is important to prevent artificial repetition of the defect in the neighboring vdW gap. For Fe_{Bi} and Fe_{Se1} our modified SC is more suitable, since it leads to a more regular (but not rectangular) SC with dimensions $12.6 \times 12.6 \times 9.4$ Å, and reduces artificial repetition within layers, where the interaction is strong. The full Brillouin zone was sampled by $5 \times 5 \times 2$ k points for hexagonal cells and $5 \times 5 \times 5$ for modified cells, and the convergence w.r.t. k-mesh density was verified. The relaxation of atomic positions around a defect was found to have important consequences for another $3d$ metal embedded in Bi_2Se_3 [29]. In the present calculations atomic positions were relaxed with a residual force criterion of 0.02 eV/Å.

Correlation effects between $3d$ electrons in Fe can roughly be described in terms of the additional Hubbard correction term U [30,31]. We have used the value $U = 3.5$–4.4 eV, which falls between the values found for bulk Fe, FeO, and its more complex oxides [32,33]. Double counting was treated in the fully localized limit, and the results were compared to plain DFT results.

We employed DFT to calculate the total energies of the system with defect(s) E^X_{tot} and the parent system E^p_{tot}. Formation energies E^X_f were then obtained from their difference corrected by the atomic chemical potentials μ_i multiplied by the number n_i of added/removed atoms i, and for the charged defects (with extra electrons q) the energy due to extra electrons [34].

$$E^X_f = E^X_f - E^p_{\text{tot}} - \sum_i n_i \mu_i + E_F q.$$

Chemical potentials depend on the growth conditions, but their values are expected to fall within certain bounds. The upper limit corresponds to the maximum concentration of the given constituent, where the potential equals the energy of the constituent in its bulk form (per atom). The lower limit (corresponding to minimum concentration) is typically imposed by subtracting the upper limit of the chemical potential of other constituents from the total energy of the complete compound. However, possible formation of other stable compounds may modify these boundaries and needs to be considered [34].

III. RESULTS AND DISCUSSION

A. HRXRD

We start our analysis with high-resolution XRD (HRXRD); for the reasoning, see Sec. B in the SM [16]. Figure 1 presents the large HRXRD $2\Theta/\omega$ scans of the investigated samples. The sharp maxima correspond to reciprocal-lattice points $000L$, where L is a multiple of 3. The measured scans were fit to a semikinematic diffraction model [35] and the basal plane distances (0001) were determined from the fits. An example of the fitting result is shown in Fig. S1 [16] for the $Fe_{0.02}Bi_2Se_3$ sample. Figure 2 shows the interplanar distances as a function of electron concentration in $Fe_xBi_2Se_3$. The interplanar distances can be a function of both the content of intercalated Fe, x, and the Fermi level. Since Fe atoms can occupy interstitial positions Fe_i, substitutional positions Fe_{Se1} (abbreviated Fe_{Se}), and Fe_{Bi}, the dependence of interplanar distances on Fe content is ambiguous.

Therefore, we use the dependence on the electron concentration. This dependence indicates that the Se1-Se1 distance decreases with n doping (presumably due to Fe_i in $Fe_xBi_2Se_3$), while the Se1-Bi distance increases. Importantly, the Bi-Se2 distance remains unchanged, suggesting that the significant point defects—either extrinsic or native—are largely located in the vdW gap or Se1 plane for $Fe_xBi_2Se_3$. Figure 2 clearly shows that the Se1 atomic layer is the most disordered, indicating a large number of defects in the vdW gap. In addition, the magnitude of the error bars for the Se1-Se1 distance is large, suggesting that the Se1-Se1 distance varies significantly between different (quintuple layer) QLs. This indicates inhomogeneously distributed impurities according to the model in Fig. 11.

Thus the HRXRD results admit defects close to the Se1-Fe interstitial, Fe_i, and substitutional positions Fe_{Se1} (extrinsic), bismuth antisites Bi_{Se1} (abbreviated Bi_{Se}), and selenium vacancies V_{Se1} (abbreviated V_{Se}) but rules out Se_{Bi}. Logically, intercalated samples are generally cation rich, leading to the formation of antisites in the anionic sublattice (Bi_{Se}) and to the disappearance of antisite defects in the cationic sublattice (Se_{Bi}) [28,36]. Note that Se_{Bi} was never observed in STM experiments. In addition, the formation energy of V_{Se} and Se_{Bi} increases with the Fermi energy E_F, making their occurrence in highly n-doped samples less likely [37]. The drop of V_{Se} and increase in Bi_{Se} in Sr-intercalated samples strongly corroborate this scenario [21]. Therefore, we exclude the Se_{Bi} and V_{Se} defects from further discussion in this case. The opposite is true for Bi_{Se}. A thorough theoretical study by Zhang *et al.* [28] clearly indicates that Bi_{Se} likely dominates

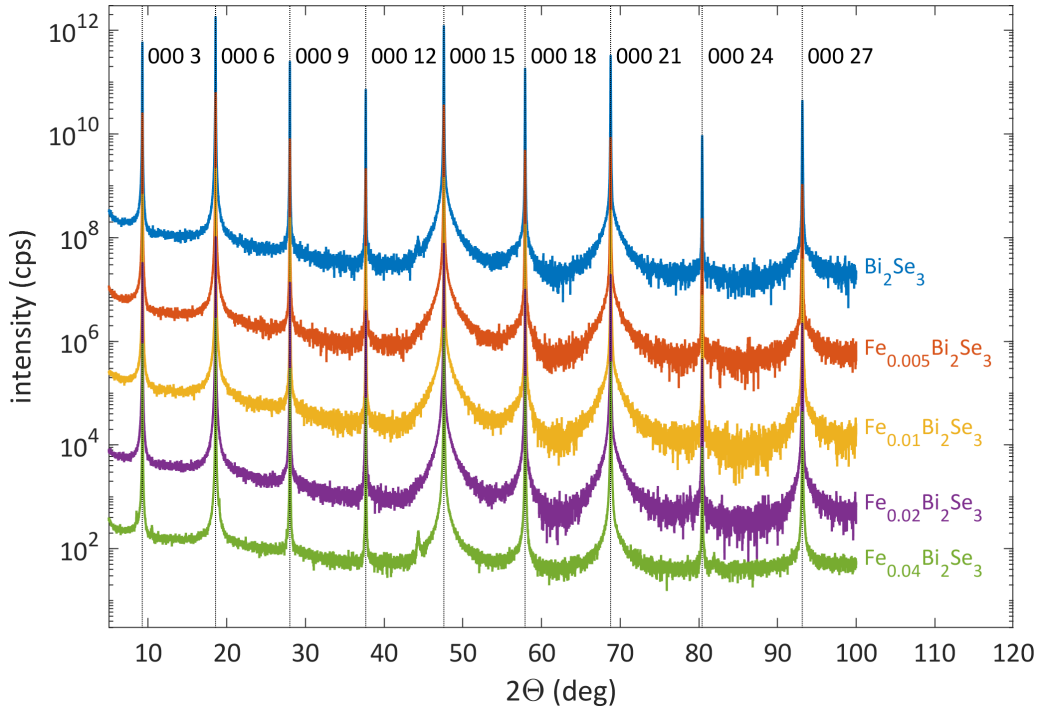

FIG. 1. HRXRD symmetric $2\Theta/\omega$ scans of all the investigated samples. The diffraction maxima $000(3n)$ are denoted by vertical dotted lines. The curves are shifted vertically for clarity.

for $Fe_xBi_2Se_3$ samples. Most importantly, the occurrence of Bi_{Se} is corroborated by core-level spectroscopy, which shows the bonding (electron transfer) of surface Fe atoms to Bi atoms of Bi_2Se_3 [38]. It follows that the surface of a QL is rich in Bi_{Se} and the Fe forms Fe_i or Fe_{Se} in $Fe_xBi_2Se_3$. The observed *n*-type doping suggests that all defects may be present depending on stoichiometry. Thus, based on HRXRD and the literature, we conclude that native defects (mainly Bi_{Se}) and external defects (mainly Fe_i), show an inhomogeneous distribution within the $Fe_xBi_2Se_3$ structure. They are mainly concentrated along the vdW gaps, but not all vdW gaps are occupied by defects equally. In other words, the coherent structure/periodicity is nicely preserved in the core of the domains, but the domain borders are often very rich in defects (Fig. 11). From the point of view of charge transport (mobility—Table I and Table SI in the SM [16]), the size of the domain and the structural perfection of the domain core are crucial. The bigger and more perfect the domain core, the better the charge transport. In other words, the occurrence of carriers with high mobility is associated with either a low concentration of defects or their segregation in the domain walls. Our DFT calculations (Sec. II) show that the formation energy of substitutional defect Fe_{Bi} increases in cation-rich samples and vice versa, which in itself prevents their formation and favors the formation of Fe_i in $Fe_xBi_2Se_3$. Thus the nominal stoichiometry largely controls the defects in the structure; we would obtain Fe_{Bi} for $Bi_{2-x}Fe_xSe_3$ (Table SI in the SM [16]) but Fe preferentially forms Fe_i and Fe_{Se} for $Fe_xBi_2Se_3$.

From the integral breadths β of the diffraction maxima depicted in Fig. 1 we estimated the vertical size D of the coherent sample domains, using the well-established Williamson-Hall plot [39], in which the values of $\beta\cos(\Theta)$ are plotted as a

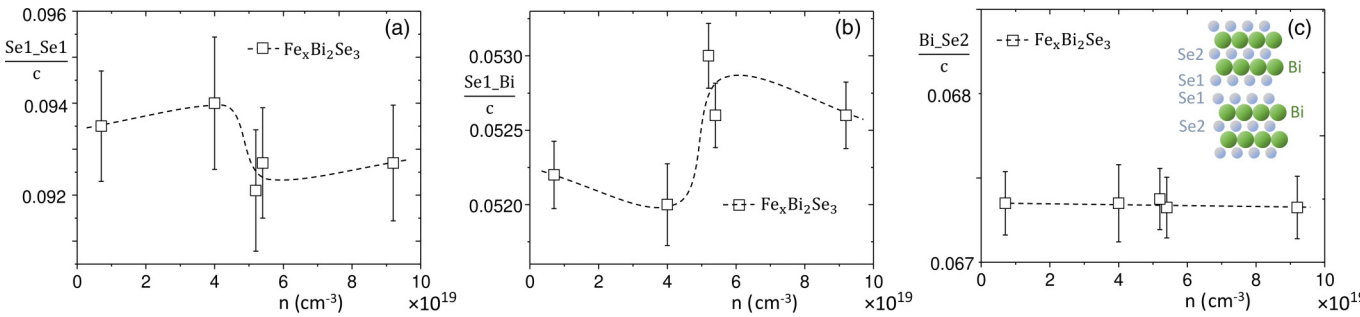

FIG. 2. Interplanar distances expressed as a fraction of the lattice parameter c in $Fe_xBi_2Se_3$ crystals as a function of electron concentration (note the axis scales). We observe sharp changes in the Se1-Se1 and Se1-Bi distances with increasing electron concentration (a,b). In contrast, the Bi-Se2-Bi structure is rigid, and insensitive to doping (c). The error bars clearly show that the most pronounced disorder occurs in the Se1 atomic layers. The electron concentration dependence shows that the critical electron concentration with respect to SC is $n \approx 4 \times 10^{19}$ cm^{-3}.

TABLE I. Transport parameters of $Fe_xBi_2Se_3$; additional doped and undoped samples are shown for comparison. DE $\approx \Delta n_{\mathrm{Hall}}/c_{\mathrm{Fe}}$ is approximate doping efficiency; $\Delta n_{\mathrm{Hall}} = n_{\mathrm{Hall}}$(sample)–$n_{\mathrm{Hall}}[Bi_2Se_3(1)]$. Bi_2Se_3 (1) is an "average" undoped stoichiometric sample and belongs to intercalated series, $Fe_xBi_2Se_3$. In addition, we present two more stoichiometric Bi_2Se_3 with border Hall concentrations within undoped Bi_2Se_3, n_{Hall}, for comparison, prepared in our laboratory [Bi_2Se_3 (2) and Bi_2Se_3 (3)]. The different transport parameters of the undoped samples of Bi_2Se_3 are related to the different quenching temperature of the single crystal. Note that samples with low concentration of electrons (i.e., defects) show similar $n_{\mathrm{SdH,3D}}$ and n_{Hall}—both methods examine the same "part" of the sample. The bulk concentration of carriers from SdH oscillations was estimated from a simplified formula for a spherical Fermi surface $n_{\mathrm{SdH,3D}} = k_F^3/3\pi^2$.

Composition	$\Delta n_{\mathrm{Hall}}/c_{\mathrm{Fe}} \approx$ DE (10^{19} cm^{-3})	SC onset in ρ_{xx} (K)	ρ_{xx} at 2 K (μΩ m)	μ_{Hall} at 2 K/300 K (cm^2 V^{-1} s^{-1})	$n_{\mathrm{SdH,3D}}$ at 2 K (10^{25} m^{-3})	n_{Hall} at 2 K (10^{25} m^{-3})	$(\mu_{\mathrm{Hall}}/c_{\mathrm{Fe}})10^{-19}$ at 2 K (cm^{-1} V^{-1} s^{-1})
$Fe_{0.005}Bi_2Se_3$	3.0/3.5 ≈ 0.86	–	0.40	3000/600	–	4.0	10500
$Fe_{0.01}Bi_2Se_3$	4.4/7.0 ≈ 0.63	2.0	0.42	2800/540	2.25	5.40	19600
$Fe_{0.02}Bi_2Se_3$	4.2/14 ≈ 0.30	3.9	0.66	1600/390	2.35	5.00	22100
$Fe_{0.04}Bi_2Se_3$	8.2/28 ≈ 0.29	5.2	0.55	1200/280	3.80	8.80	33700
$Fe_{0.1}Bi_2Se_3$	12/70 ≈ 0.17	–	0.88	680/200	–	12.6	47600
$Fe_{0.1}Bi_2Se_3$ [13]	–/ 70	6.0	3.00	–	–	–	–
Bi_2Se_3 (1)	–	–	1.54	1870 / 780	–	1.0	–
Bi_2Se_3 (2)	–	–	2.45	3700/1620	0.68	0.69	–
Bi_2Se_3 (3)	–	–	2.65	920/510	1.05	2.6	–
$Nb_{0.25}Bi_2Se_3$ [15]	24/175	3.2	0.80	≈ 150/–	2.60	24.0	–

function of sin(Θ) (Fig. 3). By extrapolating the linear part of this function to sin(Θ) → 0 we estimated the values of D to an accuracy of approximately ±10 nm. It addresses the evolution of domain thickness due to doping. Figure 4 shows the reciprocal-space maps measured in the HRXRD setup in the vicinity of reciprocal-lattice points 000 15 and 000 27. The diffraction maxima are elongated along the Debye rings (roughly in the horizontal direction). This elongation is due to lattice mosaicity, i.e., random misorientation of the crystal lattices in the mosaic subgrains (coherent domains). Since the structure of the diffraction maxima along the Debye rings is rather spotty, the lateral size of the coherent domains is large so that the number of coherent domains in the irradiated sample volume (roughly 1 mm × 2 mm × 10 μm) is small,

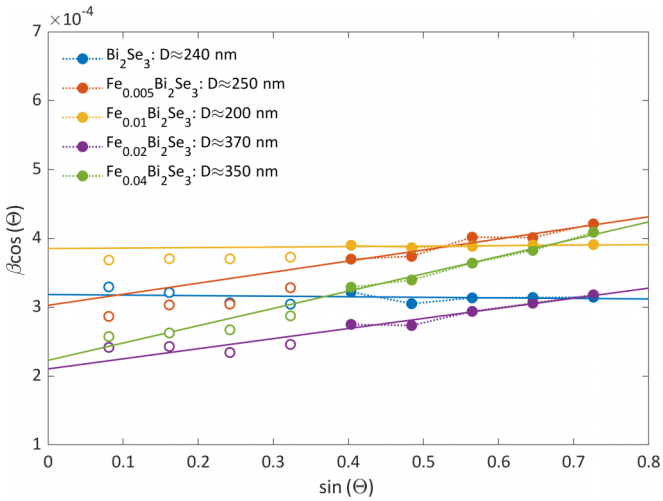

FIG. 3. The Williamson-Hall plots of the investigated samples. The experimental points are denoted by circles, the extrapolation was carried out considering the full circles, and empty circles were ignored. The estimated values of D are given in the legend.

meaning the measured signal is not statistically averaged. From this we conclude that the mean lateral domain size is quite large and most likely comparable to or even exceeding the coherent width of the incoming x-ray beam (≈1 μm). To qualitatively assess the mosaicity, we integrated the measured reciprocal-space maps in angular space in the direction perpendicular to the Debye ring (i.e., along the 2Θ-ω axis), and the results are plotted in Fig. 5. It is clear that the profiles of the integrated intensities along the angular $\phi = \omega - \Theta$ axis in diffractions 000 15 and 000 27 are very similar, suggesting that the horizontal broadening of the maxima is indeed due to angular misorientation and not due to the finiteness of the lateral domain sizes. The finite domain size would cause the same widths of the 000 15 and 000 27 maxima in the Q space (and not in the angular space).

Interestingly, the angular misorientation increases with increasing Fe content; for $x = 0.02$ and 0.04 the integrated intensity shows two maxima, indicating that the distribution of misorientations (rocking curve) has two more populated misorientations (bimodal distribution), which indicates it is not completely random. A similar rocking curve was observed for $Sr_{0.1}Bi_2Se_3$—Fig. 7 in [40].

B. DFT

To the best of our knowledge, there is a scarcity of data on the Fe substitutional defect at the Se1 site, Fe_{Se}, in the literature, and we have also not seen much relevant detailed analysis of the role of electronic correlations at Fe d electrons, which could be important in this system. Therefore, we performed first principles calculations for relevant Fe positions within the DFT+U approach, including Fe_{Se}, with a focus on the sensitivity to the inclusion of many-body effects in terms of Hubbard U. We found that correlations between localized Fe d electrons significantly affect defect formation energies; for example, those of Fe interstitials are profoundly lowered when Hubbard U is included in DFT calculations. Therefore,

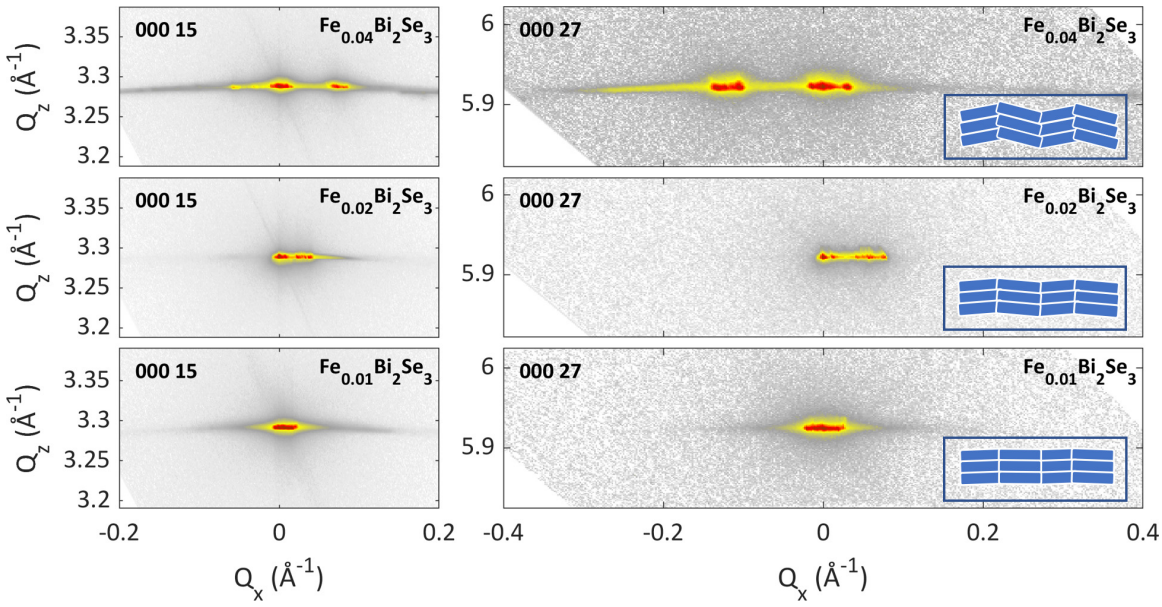

FIG. 4. Reciprocal-space maps measured around the reciprocal-lattice points 000 15 (left column) and 000 27 (right column) on $Fe_xBi_2Se_3$. The intensities are plotted logarithmically and the color scale spans over 5 decades. The insets schematically illustrate the evolution of bimodal mosaicity.

we calculated the parameters for the Fe-based point defects, but otherwise rely largely on the rich literature (see also comments in the SM [16]). Densities of states as a function of electron energy were calculated for Bi_2Se_3 with one substitutional defect Fe_{Se} (Fig. 6), one substitutional defect Fe_{Bi} (Fig. 7), or one interstitial atom Fe_i (Fig. 8) in the supercell. The positions of the Fermi level imply that Fe_{Se} and Fe_i are strong donors, while Fe_{Bi} is a weak acceptor. The defect formation energies were 2.05 for the Se-rich and 1.35 eV for the Bi-rich composition in the case of Fe_{Se}, while for Fe_{Bi} we obtained values in a similar range, namely, 1.43 eV for the Se-rich composition and 2.48 for the Bi-rich composition. From the point of view of formation energy, the occurrence of both substitutional defects is therefore almost equally likely but for opposite richness. This shows that the concentration of the substitutional defects is controlled mainly by stoichiometry.

Figure 8 shows the density of states (DOS) of Bi_2Se_3 with one interstitial atom Fe_i in the supercell. The position of the Fermi level implies that Fe_i is a strong donor. The defect

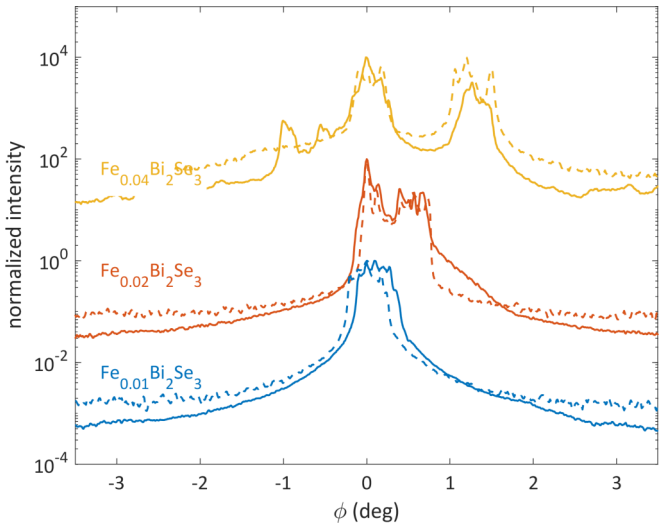

FIG. 5. The reciprocal-space maps plotted in Fig. 4 integrated in angular space in the direction perpendicular to the Debye rings. The horizontal coordinate is $\phi = \omega - \Theta$, and the full and dashed lines depict the intensities around the reciprocal-lattice points 000 15 and 000 27, respectively.

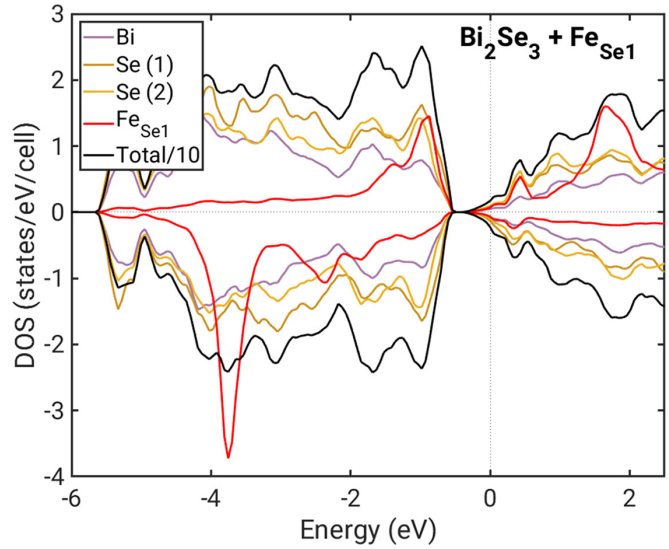

FIG. 6. DOS spectrum for Bi_2Se_3 structure with one Fe atom substituting for a Se atom in the supercell, which corresponds to substitutional defect Fe_{Se}^{+1}. The vertical line represents the Fermi level.

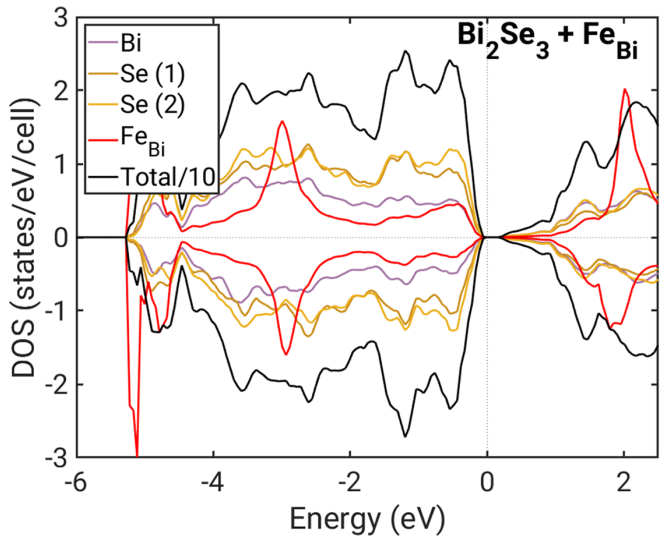

FIG. 7. DOS spectrum for Bi_2Se_3 structure with one Fe atom substituting for a Bi atom in the supercell, which corresponds to substitutional defect Fe_{Bi}^{-1}. The vertical line represents the Fermi level.

formation energies are 0.26 eV. This renders interstitial Fe to be the most probable defect in $Fe_xBi_2Se_3$.

Most likely, all defects tend to form clusters [41,42]. For example, Fe prefers Bi coordination, which implies the formation of complex defects, such as Fe_i coordinated by NBi_{Se} [38]. Thus the high concentration of defects in the Se1 layer alters the formation energies of all involved defects, which naturally induces defect clustering. In the case of layered materials, the clustering probably occurs mainly in the vdW gap. We encourage scientists with better techniques to address, for example, the problem of Fe_{Se} or Fe_i defects coordinated by Bi_{Se} defects.

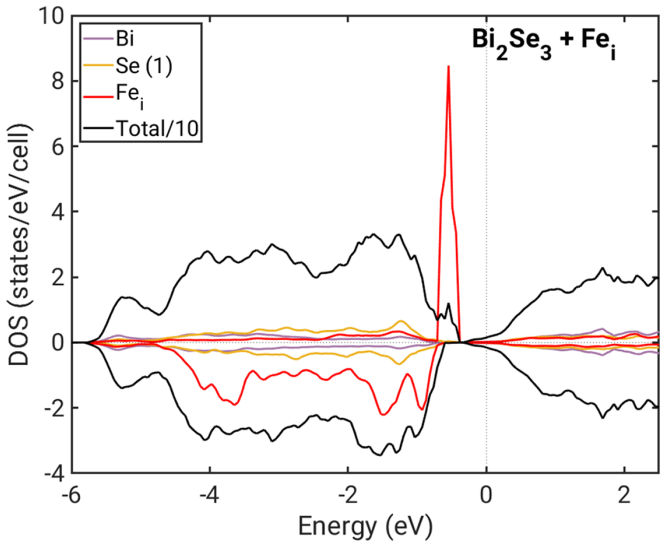

FIG. 8. DOS spectrum for Bi_2Se_3 structure with one Fe atom in the interstitial position, Fe_i^{+1}. The vertical line represents the Fermi level.

C. Transport and magnetotransport data—high carrier mobility

Charge transport parameters of $Fe_{0.02}Bi_2Se_3$ as a function of temperature/magnetic field are summarized in Figs. 9(a)–9(d), and Table I. By analyzing the SdH oscillations at $T = 2$ K, we obtained two close frequencies, $f_1 = 243$ T and $f_2 = 261$ T, reflecting the presence of two electron subbands [43]. Note that the beats in Fig. 9(d) may also be due to Rashba splitting ($\Delta E \approx 3.3$ meV), which would reflect a reduction in the symmetry of the structure due to Fe doping. The SdH oscillations can be nicely fitted within the Lifshitz-Kosevich formula (Sec. C in the SM [16]); the detailed analysis is summarized in Fig. 10. The occurrence of Hall plateaus may indicate the involvement of 2D transport at low temperatures [10,11]. In an attempt to match the Hall plateaus with SdH oscillations, we noted that a portion of the Hall conductivity must be assigned to the nonquantized Hall conductivity to obtain integer multiples of the quantum conductivity. This was left unaddressed in previous articles [10,11]. We approximated the nonquantized Hall conductivity (corresponding to 3D TnT layers discussed below within Fig. 11) using a linear function in reciprocal field strength. We present the result in Fig. 9(c) showing perfect quantization over many plateaus. Thus we conclude that in the low-temperature region, charge transport in $Fe_{0.02}Bi_2Se_3$ consists of at least nonquantized conductivity (band states) and quantized 2D conductivity. This conclusion supports the model of a nanoheterogeneous structure replicating the mosaicity of a single crystal (Fig. 11). The Fe-doped samples showed an unusually high carrier concentration compared to the average concentration of pristine material ($\approx 1.5 \times 10^{19}$ cm^{-3}) and published data on substitutionally Fe-doped samples ($\approx 1.0 \times 10^{19}$ cm^{-3}) [8]. Interestingly, we did not observe a corresponding decrease in their mobility due to doping and rising E_F. This is in sharp contrast to very low mobility of "undoped" samples that were prepared with a deliberately high concentration of defects and thus electrons; see, e.g., the results of Petrushevsky *et al.* [9], Cao *et al.* [22], and Huang *et al.* [44] and one of our samples Bi_2Se_3(3) (Table I). The rather high mobility in $Fe_xBi_2Se_3$ samples results in unusually low metallic resistivities. We address this by introducing the product of carrier mobility and Fe concentration, $\mu_H \cdot c_{Fe}$ reflecting the scattering magnitude of involved extrinsic Fe-based defects. The $\mu_H \cdot c_{Fe}$ product increases with Fe concentration up to $x = 0.1$ (Table I), indicating that Fe doping species remain at least partially "invisible" for electrons in terms of scattering. This is in line with HRXRD experiments indicating the concentration of defects along the vdW gap: Fe concentrates along domain walls while domain cores are almost defect free (the model in Fig. 11). Such a high mobility in Fe-doped samples indicates that native defects such as Bi_{Se} are also largely concentrated in the domain walls as a result of Fe doping. Second, the high mobility just at low temperatures suggests the involvement of topological surface states. Thus we assume that vdW gaps rich in Fe_i and Bi_{Se} form a TT layer which mimics the surface (TT vacuum) in topology and gives rise to Dirac states in adjacent layers throughout the volume of the crystal. Therefore, we refer to adjacent layers as 2D TnT Dirac in Fig. 11. Two-dimensional TnT

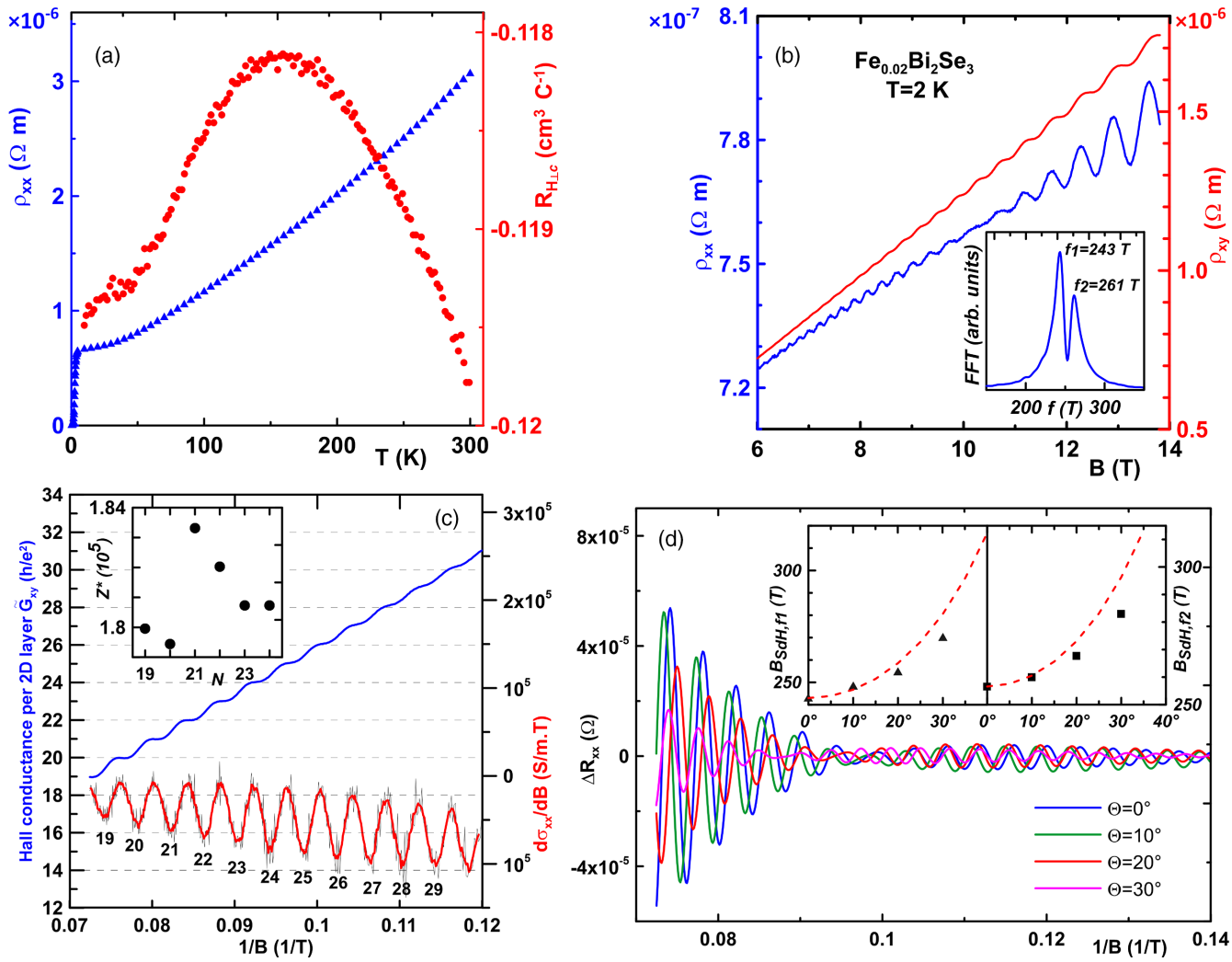

FIG. 9. (a) Longitudinal resistivity ρ_{xx} and Hall coefficient R_H of the $Fe_{0.02}Bi_2Se_3$ sample as a function of temperature. (b) Longitudinal resistivity ρ_{xx} and Hall resistivity ρ_{xy} of $Fe_{0.02}Bi_2Se_3$ sample as a function of out of plane magnetic field B; the inset presents an example of a fast Fourier transform (FFT) curve obtained from the measured SdH oscillations for the $Fe_{0.02}Bi_2Se_3$ sample. (c) Hall conductance $\tilde{G}_{xy} = G_{xy}/Z^*$ in units of e^2/h (left axis and blue curve) and $d\sigma/dB$ (right axis and red curve) vs inverse magnetic field at $T = 2$ K. The inset picture represents the calculated number of 2D layers Z^* vs Landau level (LL) index N. We believe that the figures do not reflect the true picture of the actual structure; they should only be used for comparison with previous papers [8–11]. (d) Angular dependence of SdH oscillations ($\Theta = 0°$–$30°$) vs inverse magnetic field for the $Fe_{0.02}Bi_2Se_3$ sample at 2 K. The insets represent SdH frequencies B_{SdH} (obtained by FFT—for details see the SM [16]) as functions of angle Θ. Red dashed curves represent calculated behavior for a planar 2D Fermi surface using $B^{2D}_{SdH} = B_\perp/\cos\Theta$. The experimental data deviate from a purely 2D character even for small angles, suggesting a predominance of 3D transport as opposed to Hall plateaus, which suggest 2D transport. Two-dimensional transport is also supported by measurement of specific heat capacity (Fig. 10).

layers exhibit reduced scattering amplitude due to the chirality of Dirac electrons and the odd number of band crossings in the energy spectrum [45]. The possible participation of Dirac states in the transport is further supported by the increase in the effective electron mass in the subbands $m^* \cong 0.14$ compared to $m^* \cong 0.08-0.11$ in undoped samples [43] (Fig. 10, left). As discussed below, we further assume that the Fe-rich TT layers are carriers of superconductivity abbreviated as SC TT (Fig. 11). The decrease in the room-temperature (RT) heat capacity from the Dulong-Petit value due to Fe doping suggests that there is a decrease in the dimensionality of both electrons and phonons (Fig. 10). The inhomogeneous defect distribution found in the energy-dispersive x-ray (EDX) analysis (SM, Sec. H, Fig. S13 [16]) may confirm these findings. The structure is thus partially divided into 2D-like platelets by "SC TT nanoinclusions" within domain walls, which consist of Fe defects (Fe_i, Fe_{Se}) and native defects (Bi_{Se}) located along the vdW gap (Fig. 11 and discussion of SC). Thus we assume that in $Fe_xBi_2Se_3$ crystals Fe forms mainly interstitial Fe_i defects. They are either individual in nature or composed of a few atoms for $x \leqslant 0.02$, while for $x > 0.02$ they may form larger clusters of NFe_i vdW gap (see SM, Sec. F [16]), mimicking the superconductive Fe_xSe_y phase for $x \geqslant 0.02$ as discussed below [46]. Furthermore, part of the Fe interstitial Fe can fill the V_{Se} defects to form Fe_{Se} [38]. Both forms are donors as evidenced by DFT, consistent with the experiment (Table I). We stress that the mosaiclike structure shown in Fig. 11 is in agreement with studies of other superconduct-

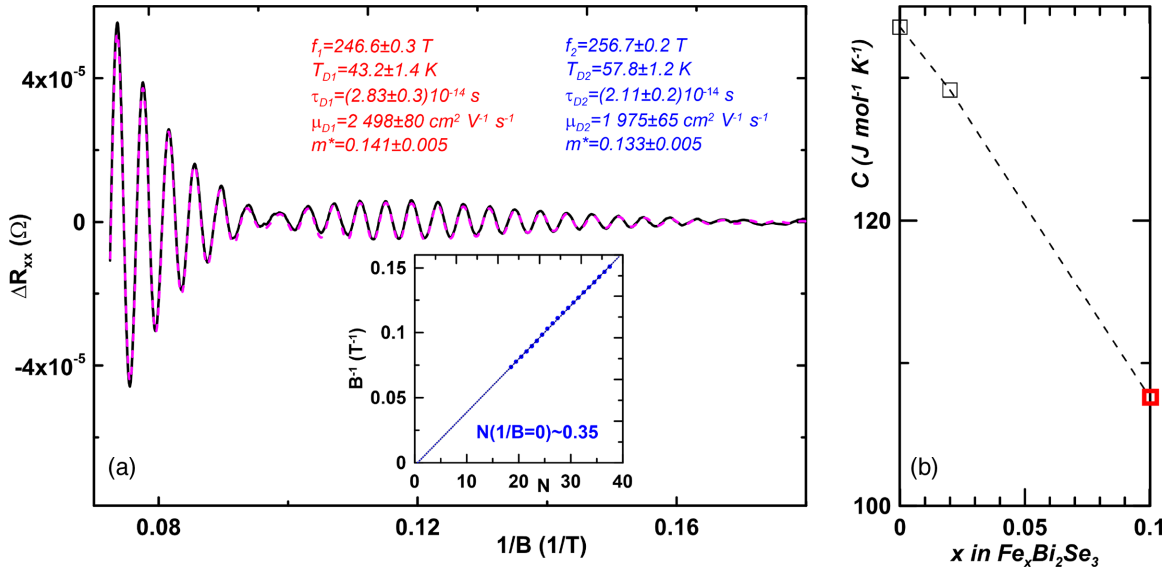

FIG. 10. $\Delta R_{xx}(1/B)$ obtained by subtracting of smooth background from $R_{xx}(1/B)$ showing pronounced beats (left). The two frequencies (f), Dingle temperatures (T_D), Dingle time (τ_D), Dingle mobilities (μ_D), and effective electron masses (m^*) are summarized in the inset column. The bottom inset depicts the fan diagram indicating the Berry phase about 0.35 of 2π. The drop of specific heat due to increasing 2D character due to Fe doping; the red square is from Ref. [13] (on the right).

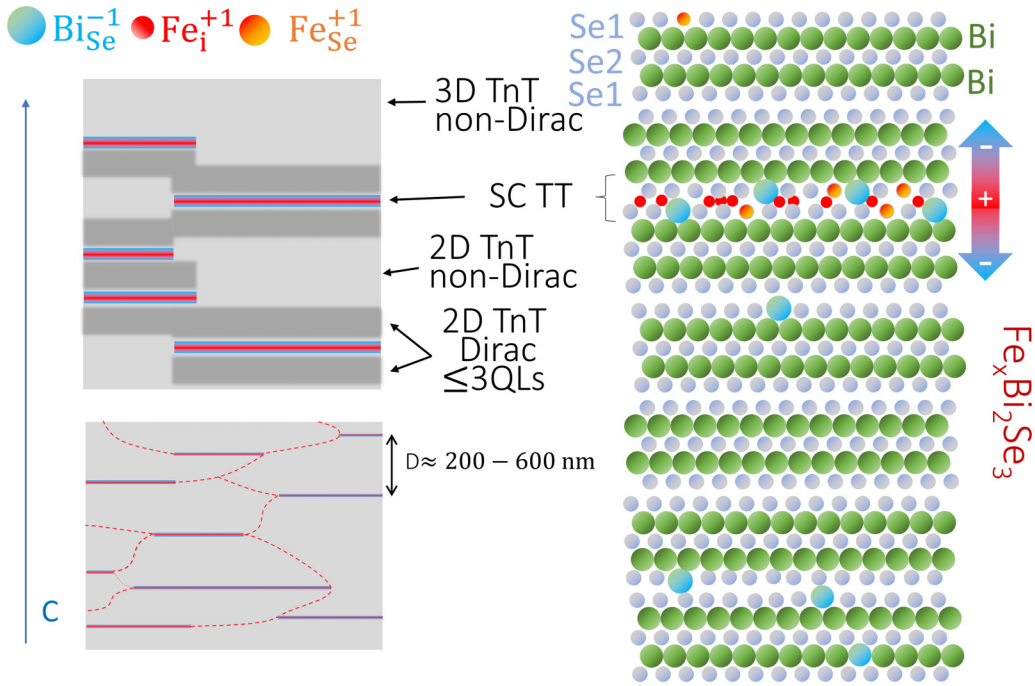

FIG. 11. (Left) A mosaiclike structure of $Fe_xBi_2Se_3$ contains superconductive topologically trivial (red-blue) SC TT layers that divide the bulk into various conducting channels (schematic cut along the c axis in the upper left corner). The topologically nontrivial Dirac states (dark gray) propagate about 2–3 QLs away from the topologically trivial (SC TT) layers [49]. The rest of the volume therefore contains either 2D (thin layers) or rather 3D (thick layers) TnT regions. Schematic image: section along the c axis of the corresponding mosaic structure described in Sec. III A, HRXRD (lower left corner). Dark gray regions corresponding to Dirac states are not shown. The thickness of the D domain depends on the doping (see Fig. 7). (Right) Detailed diagram of the TT and TnT layers within the QL structure of Bi_2Se_3. Formation of layers rich in Fe_i^{+1}, $Fe_{Se}^{+1}/Bi_{Se}^{-1}$ (SC TT) leads to decrease/increase of Se1-Se1/Se1-Bi atomic plane distances, respectively (see Sec. III A, HRXRD). Although we assume that the TT layers are SC carriers, the Dirac electrons could also mediate SC [12]. The electric field shown schematically by the arrows on the right may arise due to the occurrence of defects located along the vdW gap. This field induces a symmetry drop and may coincide with the Rashba field mentioned above. Note that $x = 0.02$ would be sufficient for one complete filling of the vdW gap with Fe atoms, i.e., creating a complete hexagonal sheet of Fe atoms every 50 QLs (≈ 150 nm). The figure is therefore schematic and the actual concentration of specific layers may be considerably lower than what is seen in the upper left corner of the figure;it is more consistent with the figure in the lower left corner.

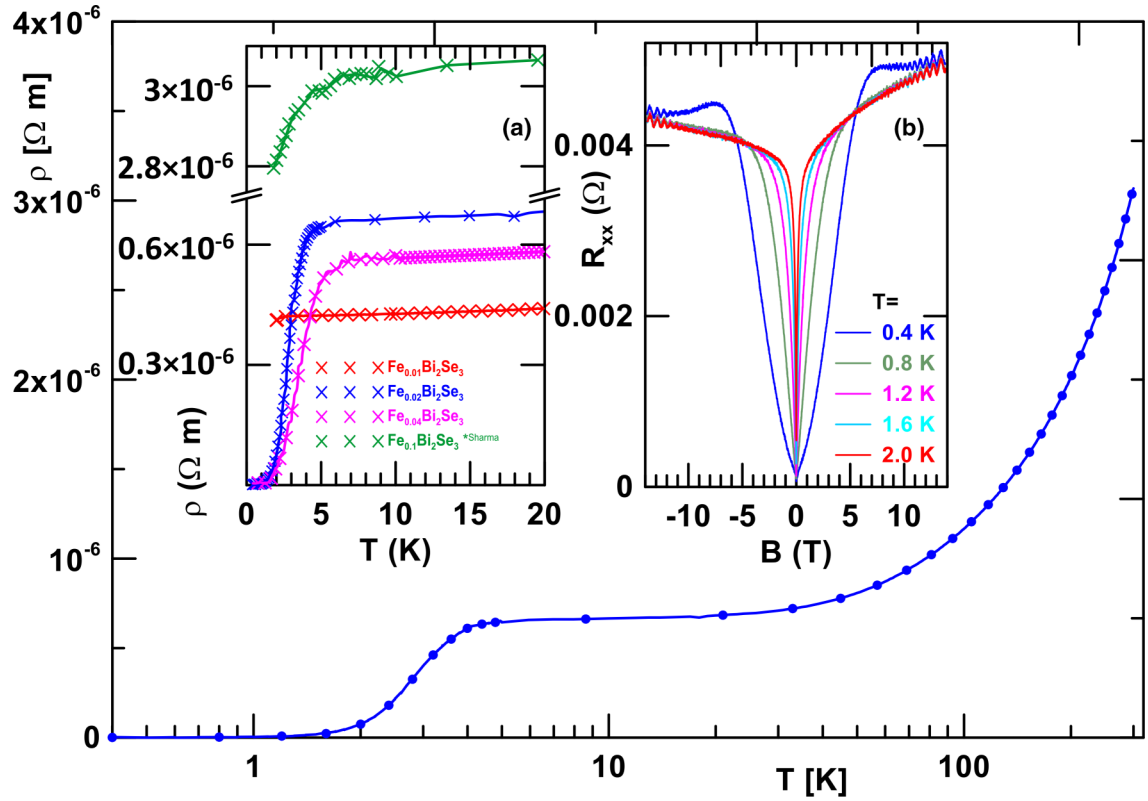

FIG. 12. The resistivity of a $Fe_{0.02}Bi_2Se_3$ crystal with applied current along the *ab* plane. The inset (a) shows the magnified view of the onsets of the superconducting transition of the studied $Fe_xBi_2Se_3$ samples ($x = 0.01, 0.02, 0.04$; detailed measurement is in the SM) compared to the published results in [13] for $Fe_{0.1}Bi_2Se_3$ composition (note the axis break). The inset (b) presents R_{xx} as a function of the out of plane magnetic field 0.4–2 K.

ing systems (Nb [47], Cu [14]). The highly defective surface for Sr-intercalated material [12,21] also shows heterogeneous structures almost identical to Fe-intercalated materials. The authors report "combination" areas with high and low concentration of nanoscopic inclusions. These experimental findings prove the occurrence of a heterogeneous layered mosaiclike system presented in Fig. 11. Such a heterogeneous 2D nanostructure along the *c* axis is similar to the structure SC cuprates [48], which is also associated with a pronounced modulation of potential [49,50]; it would therefore be consistent with the emergence of a Rashba field due to the absence of inversion symmetry. Importantly, the heterogeneous nanostructure may also explain the large discrepancy between the Hall and SdH carrier concentrations, which is very pronounced in the Nb-doped Bi_2Se_3 of Lawson *et al.* [15]. Particularly, by an order higher Hall concentration compared to SdH, concentration may be dominated by the metallic (tentatively SC) part (layer) of a mosaic structure, e.g., $Bi_2Se_3/(BiSe)_{1+\delta}NbSe_2$ [51]. The same applies to $Fe_xBi_2Se_3$ samples. The SdH oscillations persisting to high temperatures (SM, Fig. S4 [16]) reflect only the excitation of highly mobile electrons in the "defect-free" domain cores (n_{SdH} in Table I and Table SI in the SM [16]), whereas the Hall effect involves all electrons in the structure, including those in the highly disordered domain walls (n_{Hall} in Table I and Table SI in the SM [16]). Note that samples with a low concentration of electrons (i.e., defects) show similar $n_{SdH,3D}$ and n_{Hall}. In such cases, both methods examine the entire sample volume. Such a mosaiclike structure naturally includes TnT 3D states (Fig. 11). These are combined with Dirac states that extend about 3 QLs from the contact to the SC TT layer [49]. The contribution of the respective conduction channels to the transport can vary with the doping level. Although not conclusive, EDX analysis suggests an inhomogeneous composition in the sample volume that may lead to the formation of conductive channels (SM, Fig. S13 [16]).

D. Superconductivity

The drop of longitudinal resistance to zero is shown in Fig. 12 for the $Fe_{0.02}Bi_2Se_3$ sample, showing the critical temperature of our SC state, $T_C \leqslant 2$ K. We observed no corresponding Meissner effect around T_C. In addition, we observed no jump in heat capacity attributable to the SC state (see .G of the SM [16]). Thus the SC volume ratio (shading ratio) is too low and the SC state is limited to a fine net of domain walls, and it is far from perfect in bulk (Fig. 11). Importantly, we exclude the possibility of the presence of a macroscopic SC Fe_xSe_y phase that would be able to "short-circuit" Bi_2Se_3 samples (see also Secs. B and H in the SM [16]). Firstly, the T_C of the superconducting Fe_xSe_y is much higher, approximately 8 K [46]. Secondly, the foreign phase FeSe appears only at high iron concentrations. The FeSe phase occurs in an islandlike fashion and precludes percolation and induction of bulk superconductivity even for $x = 0.1$. Thus, thirdly, it is very unlikely that this phase would be able to short-circuit all

samples (i.e., to reach percolation limit) for $x = 0.02$ (SM, Sec. H [16]). Importantly, higher doping levels ($x > 0.04$) even prevent the zero-resistance state from being reached, which is inconsistent with the SC state induced by extraneous phase Fe_xSe_y. Fourthly, there are no traces of extraneous Fe-containing phases in reciprocal-space mapping for $x \leqslant 0.04$ (see Sec. B in the SM [16]). Thus the culprits for the drop in resistance to zero are the SC TT layers—domain walls associated with the mosaicity of the single crystals. Although it may be a layer structurally related to tetragonal FeSe in terms of SC, it is another "2D" phase. The proximity-induced SC in Bi_2Se_3 also corroborates our conclusion [52].

To our knowledge, there are four dopants capable of inducing SC in bulk Bi_2Se_3, namely, Cu [14], Nb [15], Sr [17], and Fe. The recent paper by Le *et al.* shows that a minute amount of Ag atoms injected into the Bi_2Se_3 vdW gap is able to locally induce SC at very low temperatures [53]. These dopants all have several features in common, one of which is a heterogeneous structure characterized by the formation of defects or even inclusions along the vdW gap. Another common point is the critical temperature which is around 3 K for all materials (very remarkable, even though it may be a coincidence). Furthermore, all dopants induce a high concentration of electrons, but the concentration spans one order of magnitude; for Sr-doped samples it may be as low as $2 \times 10^{19}\,\mathrm{cm}^{-3}$ while for Nb-doped samples $n \approx 2 \times 10^{20}\,\mathrm{cm}^{-3}$ [15]. Therefore, the electron concentration alone cannot account for the SC state. On the contrary, the comparison strongly suggests that there must be another feature common to all Bi_2Se_3-based SC materials. The experimental and theoretical findings indicate that this feature common to SC is the defect structure—a fine mosaiclike structure in the case of Fe and possibly Sr, but most likely a rough one in the case of Cu and Nb.

Within the fine mosaiclike 2D nanostructure of $Fe_xBi_2Se_3$, the bottom limit concentration of Fe_i^{+1}, $Fe_{Se}^{+1}/Bi_{Se}^{-1}$, may be defined by the ability of Cooper pairs of SC TT regions (Fig. 11) to overcome the non-SC areas within the proximity-induced superconductivity ($x < 0.02$) [52]. The possible unconventional nature of the SC state has yet to be proven.

IV. CONCLUSION

We explored the structural and transport properties of $Fe_xBi_2Se_3$ single crystals. $Fe_xBi_2Se_3$ shows an extraordinarily high mobility, features of 2D transport, and weak superconductivity. It differs significantly from earlier Bi_2Se_3-based superconductors in the relatively low concentration of the doping element ($x = 0.02$). Although the argument in the paper may seem uncomfortably complex, the basic idea of superconductivity, high mobility, and 2D transport in $Fe_xBi_2Se_3$ that emerges from this argument is simple. All effects are associated with the special defect structure of Bi_2Se_3. This defect structure largely replicates, or rather forms, the domain structure—i.e., reflects the mosaicity of single crystals. Some domain walls are rich in defects, while the domain cores remain largely defect free, ensuring high electron mobility and thus occurrence of the SdH effect. Moreover, Fe-rich domain walls can become superconducting. Thus, in our case, superconductivity is weak because it consists only of a fine network of superconducting domain walls largely along the vdW gap—Fe_i^{+1}, $Fe_{Se}^{+1}/Bi_{Se}^{-1}$ defects collect along the vdW gap and thus form a superconducting network. In addition, they may form a potential barrier due to charging. This gives the structure a somewhat 2D character in terms of charge and heat transport. The appearance of the 2D features depends on the size and concentration of the barriers—domain walls. Because these barriers can become topologically trivial, they can additionally increase the participation of Dirac electrons in bulk charge transfer. Specifically, such barriers increase the number of interfaces between topologically trivial and topologically nontrivial regions (TT/TnT), thus promoting Dirac-like transport in bulk. This explains the different Berry phases observed for different samples in the literature. We show that when analyzing the physical properties of doped and undoped Bi_2Se_3 single crystals, their domain structure should always be taken into account. Indeed, it may be an important component of many effects and "unknowns" observed in this material. Moreover, such a doping-enhanced nanostructure may be advantageous for TE properties in terms of mobility and energy filtering of electrons.

ACKNOWLEDGMENTS

This work was supported by the Grant Agency of the Czech Republic (Project No. 19-16315S). Experiments were performed in MGML (mgml.eu), which is supported within the program of Czech Research Infrastructures (Project No. LM2018096). V.H. acknowledges the support of the project NanoCent financed by the European Regional Development Fund (Project No. CZ.02.1.01 /0.0/0.0/15.003/0000485). We acknowledge Center for Computational Materials Science, Institute for Materials Research, Tohoku University for the use of MASAMUNE-IMR (Project No. 2212SC0510). We are grateful to prof. Ernst Bauer for fruitful discussions

[1] K. Hashimoto, Galvanomagnetic effects in bismuth selenide Bi_2Se_3, J. Phys. Soc. Jpn. **16**, 1970 (1961).

[2] T. Dietl, H. Ohno, and F. Matsukura, Hole-mediated ferromagnetism in tetrahedrally coordinated semiconductors, Phys. Rev. B **63**, 195205 (2001).

[3] D. Hsieh, Y. Xia, D. Qian, L. Wray, J. H. Dil, F. Meier, J. Osterwalder, L. Patthey, J. G. Checkelsky, N. P. Ong *et al.*, A tunable topological insulator in the spin helical Dirac transport regime, Nature (London) **460**, 1101 (2009).

[4] M. Z. Hasan and C. L. Kane, Colloquium: Topological insulators, Rev. Mod. Phys. **82**, 3045 (2010).

[5] S. Yonezawa, Bulk topological superconductors, arXiv:1604.07930.

[6] K. Matano, M. Kriener, K. Segawa, Y. Ando, and G. Q. Zheng, Spin-rotation symmetry breaking in the superconducting state of $Cu_xBi_2Se_3$, Nat. Phys. **12**, 852 (2016).

[7] S. Yonezawa, Nematic superconductivity in doped Bi_2Se_3 topological superconductors, Condens. Matter **4**, 2 (2019).

[8] J. Ge, T. Chen, M. Gao, X. Wang, X. Pan, M. Tang, B. Zhao, J. Du, F. Song, Y. Xu *et al.*, Evidence of layered transport of bulk carriers in Fe-doped Bi_2Se_3 topological insulators, Solid State Commun. **211**, 29 (2015).

[9] M. Petrushevsky, E. Lahoud, A. Ron, E. Maniv, I. Diamant, I. Neder, S. Wiedmann, V. K. Guduru, F. Chiappini, U. Zeitler *et al.*, Probing the surface states in Bi_2Se_3 using the Shubnikov-de Haas effect, Phys. Rev. B **86**, 045131 (2012).

[10] O. Chiatti, C. Riha, D. Lawrenz, M. Busch, S. Dusari, J. Sánchez-Barriga, A. Mogilatenko, L. V. Yashina, S. Valencia, A. A. Ünal *et al.*, 2D layered transport properties from topological insulator Bi_2Se_3 single crystals and micro flakes, Sci. Rep. **6**, 27483 (2016).

[11] M. Busch, O. Chiatti, S. Pezzini, S. Wiedmann, J. Sánchez-Barriga, O. Rader, L. V. Yashina, and S. F. Fischer, High-temperature quantum oscillations of the Hall resistance in bulk Bi_2Se_3, Sci. Rep. **8**, 485 (2018).

[12] G. Du, J. Shao, X. Yang, Z. Du, D. Fang, J. Wang, K. Ran, J. Wen, C. Zhang, H. Yang *et al.*, Drive the Dirac electrons into Cooper pairs in $Sr_xBi_2Se_3$, Nat. Commun. **8**, 14466 (2017).

[13] S. Sharma and C. S. Yadav, Electronic transport properties of Fe intercalated Bi_2Se_3 compound: $Fe_{0.10}Bi_2Se_3$, in *Advanced Materials: Proceedings of the International Workshop on Advanced Materials (IWAM-2017)*, AIP Conf. Proc. No. 2005 (AIP, Melville, NY, 2018), p. 040006.

[14] Y. S. Hor, A. J. Williams, J. G. Checkelsky, P. Roushan, J. Seo, Q. Xu, H. W. Zandbergen, A. Yazdani, N. P. Ong, and R. J. Cava, Superconductivity in $Cu_xBi_2Se_3$ and its Implications for Pairing in the Undoped Topological Insulator, Phys. Rev. Lett. **104**, 057001 (2010).

[15] B. J. Lawson, P. Corbae, G. Li, F. Yu, T. Asaba, C. Tinsman, Y. Qiu, J. E. Medvedeva, Y. S. Hor, and L. Li, Multiple Fermi surfaces in superconducting Nb-doped Bi_2Se_3, Phys. Rev. B **94**, 041114(R) (2016).

[16] See Supplemental Material at http://link.aps.org/supplemental/10.1103/PhysRevB.108.125308 for DFT calculations (Sec. A), HRXRD analysis (Sec. B), analysis of Shubnikov–de Haas oscillations (Sec. C), sample preparation and superconductivity (Sec. D), atomic force microscopy (Sec. E), and low-temperature susceptibility and magnetization.

[17] Z. Liu, X. Yao, J. Shao, M. Zuo, L. Pi, S. Tan, C. Zhang, and Y. Zhang, Superconductivity with topological surface state in $Sr_xBi_2Se_3$, J. Am. Chem. Soc. **137**, 10512 (2015).

[18] V. K. Maurya Shruti, P. Neha, P. Srivastava, and S. Patnaik, Superconductivity by Sr intercalation in the layered topological insulator Bi_2Se_3, Phys. Rev. B **92**, 020506(R) (2015).

[19] C. Q. Han, H. Li, W. J. Chen, F. Zhu, M.-Y. Yao, Z. J. Li, M. Wang, B. F. Gao, D. D. Guan, C. Liu *et al.*, Electronic structure of a superconducting topological insulator Sr-doped Bi_2Se_3, Appl. Phys. Lett. **107**, 171602 (2015).

[20] K. Willa, R. Willa, K. W. Song, G. D. Gu, J. A. Schneeloch, R. Zhong, A. E. Koshelev, W. K. Kwok, and U. Welp, Nanocalorimetric evidence for nematic superconductivity in the doped topological insulator $Sr_{0.1}Bi_2Se_3$, Phys. Rev. B **98**, 184509 (2018).

[21] Y. R. Lin, M. Bagchi, S. Soubatch, T. L. Lee, J. Brede, F. C. Bocquet, C. Kumpf, Y. Ando, and F. S. Tautz, Vertical position of Sr dopants in the $Sr_xBi_2Se_3$ superconductor, Phys. Rev. B **104**, 054506 (2021).

[22] H. Cao, J. Tian, I. Miotkowski, T. Shen, J. Hu, S. Qiao, and Y. P. Chen, Quantized Hall effect and Shubnikov–de Haas oscillations in highly doped Bi_2Se_3: Evidence for layered transport of bulk carriers, Phys. Rev. Lett. **108**, 216803 (2012).

[23] A. P. Torane, C. D. Lokhande, P. S. Patil, and C. H. Bhosale, Preparation and characterization of electrodeposited Bi_2Se_3 thin films, Mater. Chem. Phys. **55**, 51 (1998).

[24] P. Lostak, Č. Drašar, I. Klichová, J. Navrátil, and T. Černohorský, Properties of Bi_2Se_3 single crystals doped with Fe atoms, Phys. Status Solidi B **200**, 289 (1997).

[25] J. Prokleška, J. Pospíšil, J. V. Poltierová, V. Sechovský, and J. Šebek, Low temperature ac susceptibility of UCoGe crystals, J. Phys.: Conf. Ser. **200**, 012161 (2010).

[26] J. K. Dewhurst, ELK code, Version 8.3.22, http://elk.sourceforge.net/.

[27] J. P. Perdew, K. Burke, and M. Ernzerhof, Generalized Gradient Approximation Made Simple, Phys. Rev. Lett. **77**, 3865 (1996).

[28] J. M. Zhang, W. M. Ming, Z. G. Huang, G. B. Liu, X. F. Kou, Y. B. Fan, K. L. Wang, and Y. G. Yao, Stability, electronic, and magnetic properties of the magnetically doped topological insulators Bi_2Se_3, Bi_2Te_3, and Sb_2Te_3, Phys. Rev. B **88**, 235131 (2013).

[29] K. Carva, P. Baláž, J. Šebesta, I. Turek, J. Kudrnovský, F. Máca, V. Drchal, J. Chico, V. Sechovský, and J. Honolka, Magnetic properties of Mn-doped Bi_2Se_3 topological insulators: *Ab initio* calculations, Phys. Rev. B **101**, 054428 (2020).

[30] V. I. Anisimov, J. Zaanen, and O. K. Andersen, Band theory and Mott insulators: Hubbard U instead of Stoner I, Phys. Rev. B **44**, 943 (1991).

[31] V. I. Anisimov, F. Aryasetiawan, and A. I. Lichtenstein, First-principles calculations of the electronic structure and spectra of strongly correlated systems: The LDA + U method, J. Phys.: Condens. Matter **9**, 767 (1997).

[32] M. Capdevila-Cortada, Z. Łodziana, and N. López, Performance of DFT+U approaches in the study of catalytic materials, ACS Catal. **6**, 8370 (2016).

[33] M. Cococcioni and S. De Gironcoli, Linear response approach to the calculation of the effective interaction parameters in the LDA+U method, Phys. Rev. B **71**, 035105 (2005).

[34] C. G. Van de Walle and J. Neugebauer, First-principles calculations for defects and impurities: Applications to III-nitrides, J. Appl. Phys. **95**, 3851 (2004).

[35] U. Pietsch, V. Holy, and T. Baumbach, *High-Resolution X-Ray Scattering: From Thin Films to Lateral Nanostructures* (Springer-Verlag, Berlin, 2004).

[36] S. Wang and P. Zhang, Native point defects in Bi_2Se_3: A first-principles study, Phys. Lett. A **384**, 126281 (2020).

[37] L. Xue, P. Zhou, C. X. Zhang, C. Y. He, G. L. Hao, L. Z. Sun, and J. X. Zhong, First-principles study of native point defects in Bi_2Se_3, AIP Adv. **3**, 052105 (2013).

[38] M. R. Scholz, J. Sánchez-Barriga, D. Marchenko, A. Varykhalov, A. Volykhov, L. V. Yashina, and O. Rader, Tolerance of Topological Surface States Towards Magnetic Moments: Fe on Bi_2Se_3, Phys. Rev. Lett. **108**, 256810 (2012).

[39] G. K. Williamson and W. H. Hall, X-ray line broadening from filed aluminium and wolfram, Acta Metall. **1**, 22 (1953).

[40] M. P. Smylie, K. Willa, H. Claus, A. E. Koshelev, K. W. Song, W. K. Kwok, Z. Islam, G. D. Gu, J. A. Schneeloch, R. D. Zhong *et al.*, Superconducting and normal-state anisotropy of

the doped topological insulator $Sr_{0.1}Bi_2Se_3$, Sci. Rep. **8**, 7666 (2018).

[41] K. Sraitrova, J. Cizek, V. Holy, T. Plechacek, L. Benes, M. Jarosova, V. Kucek, and C. Drasar, Vacancies in SnSe single crystals in a near-equilibrium state, Phys. Rev. B **99**, 035306 (2019).

[42] K. C. Sraitrova, J. Cizek, V. Holy, J. Kasparova, T. Plechacek, V. Kucek, J. Navratil, A. Krejcova, and C. Drasar, As-doped SnSe single crystals: Ambivalent doping and interaction with intrinsic defects, Phys. Rev. B **103**, 085203 (2021).

[43] V. A. Kulbachinskii, N. Miura, H. Nakagawa, H. Arimoto, T. Ikaida, P. Lostak, and C. Drasar, Conduction-band structure of $Bi_{2-x}Sb_xSe_3$ mixed crystals by Shubnikov–de Haas and cyclotron resonance measurements in high magnetic fields, Phys. Rev. B **59**, 15733 (1999).

[44] F. T. Huang, M. W. Chu, H. H. Kung, W. L. Lee, R. Sankar, S. C. Liou, K. K. Wu, Y. K. Kuo, and F. C. Chou, Nonstoichiometric doping and Bi antisite defect in single crystal Bi_2Se_3, Phys. Rev. B **86**, 081104(R) (2012).

[45] J. Seo, P. Roushan, H. Beidenkopf, Y. S. Hor, R. J. Cava, and A. Yazdani, Transmission of topological surface states through surface barriers, Nature (London) **466**, 343 (2010).

[46] F. C. Hsu, J. Y. Luo, K. W. Yeh, T. K. Chen, T. W. Huang, P. M. Wu, Y. C. Lee, Y. L. Huang, Y. Y. Chu, D. C. Yan *et al.*, Superconductivity in the PbO-type structure α-FeSe, Proc. Natl. Acad. Sci. USA **105**, 14262 (2008).

[47] Y. Qiu, K. N. Sanders, J. Dai, J. E. Medvedeva, W. Wu, P. Ghaemi, T. Vojta, and Y. S. Hor, Time reversal symmetry breaking superconductivity in topological materials, arXiv:1512.03519.

[48] M. Vojta, Lattice symmetry breaking in cuprate superconductors: Stripes, nematics, and superconductivity, Adv. Phys. **58**, 699 (2009).

[49] P. Rakyta, B. Ujfalussy, and L. Szunyogh, Band bending at the surface of Bi_2Se_3 studied from first principles, New J. Phys. **17**, 123011 (2015).

[50] K. Sumida, M. Kakoki, J. Reimann, M. Nurmamat, S. Goto, Y. Takeda, Y. Saitoh, K. A. Kokh, O. E. Tereshchenko, J. Güdde *et al.*, Magnetic-impurity-induced modifications to ultrafast carrier dynamics in the ferromagnetic topological insulators $Sb_{2-x}V_xTe_3$, New J. Phys. **21**, 093006 (2019).

[51] K. J. Dalgaard, S. M. Kevy, L. Wollesen, Q. Ma, S. Wiedmann, K. G. V. S. Clauss, and M. Bremholm, Local structure of Nb in superconducting Nb-doped Bi_2Se_3, Phys. Rev. B **103**, 184103 (2021).

[52] Y. Zhang, W. M. Zhao, C. Zhang, P. Wang, T. Wang, S. C. Li, Z. Xing, and D. Xing, Anomalous superconducting proximity effect in $Bi_2Se_3/FeSe_{0.5}Te_{0.5}$ thin-film heterojunctions, Adv. Mater. **34**, 2107799 (2022).

[53] T. Le, Q. Ye, C. Chen, L. Yin, D. Zhang, X. Wang, and X. Lu, Erasable superconductivity in topological insulator Bi_2Se_3 induced by voltage pulse, Adv. Quantum Technol. **4**, 2100067 (2021).